



Influence of the solvent on the structure, morphology and performance for H₂ evolution of CdS photocatalysts prepared by solvothermal method

F. Vaquero, R.M. Navarro*, J.L.G. Fierro

Instituto de Catálisis y Petroleoquímica, CSIC, C/Marie Curie 2, Cantoblanco, 28049 Madrid, Spain

ARTICLE INFO

Article history:

Received 27 June 2016

Received in revised form 21 October 2016

Accepted 26 October 2016

Available online 27 October 2016

Keywords:

CdS

Morphology

Solvent

Solvothermal

Hydrogen production

Photocatalyst

ABSTRACT

CdS crystals with different morphologies, nanorods, sheets, microspheres and irregular particles have been obtained by changing the solvothermal solvent (ethylenediamine, diethylenetriamine, triethanolamine and ethanol). Characteristics of the solvothermal solvents, such as dielectric constant, ion-coordination and length of an atomic chain, have influence on the nucleation and growth of CdS crystals. The differences in the morphological and structural characteristics of the CdS crystals have strong influence on their photophysical properties as well as in their photoactivity for hydrogen production under visible light from aqueous solutions containing Na₂SO₃ and Na₂S as sacrificial electron donor agents. The hydrogen production rate on CdS samples decreases in the order: nanorods (ethylenediamine) > sheets (diethylenetriamine) > irregular particles (triethanolamine) » microspheres (ethanol). Variations in photoactivity were analysed taking into account the changes in the morphology, structure, surface and light absorption ability of CdS crystals.

© 2016 Elsevier B.V. All rights reserved.

1. Introduction

Photocatalytic hydrogen evolution from water splitting using semiconductor photocatalysts is of great interest for the conversion of solar energy into chemical energy [1–3]. To date, many oxides, sulfides, oxynitrides and oxysulfides have been found to be active for hydrogen production from water splitting under visible light irradiation. However, the efficiency values achieved are still far from the quantum yield of 10% marked as the initial starting point for practical application [4–7]. Chalcogenides are considered as good candidates for photocatalytic hydrogen production due to its suitable band gap and the position of their conduction and valence bands [8,9]. Among chalcogenides, CdS is probably one of the most studied photocatalyst because it has a relatively narrow band gap (2.40 eV) that corresponds well with the spectrum of sunlight [10–13]. It is well known that the photocatalytic activity of CdS nanocrystals is strongly dependent on its morphology, crystalline structure, specific surface area, and crystalline size [14]. These factors determine the band gap structure, the light absorption ability, the charge-carrier separation and transport and the reactions on the surface. High photocatalytic efficiency of CdS is associated with

hexagonal phase, high crystallinity, short bulk-to-surface diffusion distance for photogenerated charges and high specific surface area. Therefore, many studies have been published in order to control the synthesis of CdS at nanometric scale [9,15,16]. The control of CdS at nanometric scale has been achieved using several methods of synthesis, including ultrasonic microemulsion [17], electrochemical synthesis [18], chemical bath deposition [19], chemical vapor deposition (CVD) [20], vapor-liquid-solid (VLS)-assisted method [21], hydrothermal [22] and solvothermal method [23]. Among the methods of synthesis listed previously, the solvothermal method is one of the most used to synthesize CdS nanocrystals due to its simplicity. Solvothermal variables such as temperature, time, precursors, molar concentration and solvent play a fundamental role in the nanostructure and morphology developed by the CdS crystals [24–27]. By careful control of the solvothermal variables it is possible to obtain CdS nanocrystals with well-controlled size and shape [28,29]. Numerous works on solvothermal synthesis of nanostructures of CdS with different morphologies (nanowires, nanorods, nanofibers, nanoflowers, nanotrees, three-dimensional dendritic, microspheres, ...) have been published in the literature [30–40]. To date, although CdS nanomaterials with different solvothermal temperature and time have been synthesized and investigated, the effect of the nature of solvent has only received limited attention. In solvothermal synthesis, the solvent can play different roles through its physico-chemical properties [38]: (i) it can control the concen-

* Corresponding author.

E-mail address: r.navarro@icp.csic.es (R.M. Navarro).

tration of the chemical species in the solution affecting the kinetics of the crystal growth, and (ii) it can modify the coordination of solvated species inducing specific nanostructures. The influence of ethylenediamine or mixed H₂O/ethylenediamine solvents on the morphology of CdS nanoparticles was studied by Zhao et al. [39]. Without ethylenediamine, CdS with spherical morphology was obtained, while with the addition of ethylenediamine CdS growth along the [001] direction was observed. Li et al. [22] reported the formation of CdS nanorods via solvothermal method with different ethylenediamine to Cd²⁺ molar ratios. Lang et al. [40] also studied the solvothermal synthesis of CdS nanostructures with different ethylenediamine/ethylene glycol mixtures and reported the synergistic effect of the control in crystalline phase and morphology of CdS to improve its photocatalytic hydrogen production. The above mentioned works are small examples which demonstrate that the selection of the solvothermal solvent can control the structure and define the morphology of the CdS nanocrystallites. In this scenario, the present work was undertaken with the aim to investigate the influence of the chemical nature of the solvent (ethylenediamine, diethylenetriamine, triethanolamine and ethanol) on the morphological, structural and optical properties of the CdS photocatalysts prepared by solvothermal method. Textural, structural and surface properties of the prepared CdS samples have been determined and related to the photoactivity results in the production of H₂ under visible light from aqueous solutions containing Na₂SO₃ and Na₂S as sacrificial electron donor agents.

2. Experimental

2.1. Solvothermal synthesis of CdS

All reagents (analytical grade) were used without further purification. In a typical preparation process, 0.0104 mol of cadmium acetate dihydrate (Cd(CH₃COO)₂·2H₂O) and 0.0312 mol of thiourea (NH₂CSNH₂) were added into a Teflon-lined stainless steel autoclave filled with ethylenediamine (EDA) to 80% of its capacity (125 mL). Water was also added (thiourea/water = 1/2 mol/mol) to produce S²⁻ anions from the thermal hydrolysis of thiourea [28,29]. The autoclave was heated in an oven at 120 °C for 12 h and left to cool down to room temperature. The yellow precipitates of CdS were collected by centrifugation, washed with distilled water and with absolute ethanol to remove the excess of solvent, and finally dried under vacuum at 70 °C for 2 h.

To investigate the effect of the chemical nature of the solvents on the morphology and crystal structure of CdS, similar solvothermal preparations were also carried out using diethylenetriamine (DETA), triethanolamine (TEA) and ethanol (EtOH) as solvents. According to the solvent used in the synthesis, samples were labelled as CdS-*x* (*x* = EtOH, TEA, EDA and DETA).

2.2. Physicochemical characterization

X-ray powder diffraction patterns of CdS-*x* samples were recorded using an X'Pert Pro PANalytical polycrystal diffractometer with an X'Celerator RTMS detector and nickel-filtered Cu Kα₁ radiation (λ = 0.15406 nm, 45 kV, 40 mA) under constant instrument parameters. For each sample, Bragg angles between 4° and 90° (2θ) were scanned with a step size of 0.0335°. Quantitative estimation of CdS primary crystallite length and width was calculated by applying the Debye-Scherrer equation from the broadening of the (002) and (101) reflections respectively.

The surface morphology and size of CdS-*x* samples were observed by Field Emission Scanning Electron Microscopy (FE-SEM) using a Philips XL30 S-FEG Microscope. The nanomorphological characteristics of CdS-*x* samples were obtained by transmission

electron microscopy (TEM) and high-resolution transmission electron microscopy (HRTEM) with a TEM/STEM JEOL 2100F operating at 200 kV accelerating voltage with a Field Emission Gun (FEG), obtaining a point resolution of 0.19 nm.

The specific surface areas of CdS-*x* samples were calculated by applying the BET method to the N₂ adsorption/desorption isotherms measured at liquid nitrogen temperature (−196 °C) on a Micromeritics TRISTAR 3000 instrument on samples previously degassed under vacuum (ca. 10^{−4} mbar) at 120 °C for 2 h to remove all gases adsorbed on their surfaces. The specific surface area values were calculated by applying the BET equation to the nitrogen adsorption isotherm within the relative pressures 0.05 < P/P₀ < 0.30. Desorption data were used to determinate the pore size distribution by the Barrett-Joyner-Halenda (BJH) method, assuming a cylindrical pore model.

X-ray photoelectron spectroscopy (XPS) measurements were acquired on a VG ESCALAB 200 R spectrometer equipped with a hemispherical electron analyzer and an Al Kα 120 W X-ray source (hν = 1486.6 eV, 1 eV = 1.6302 × 10^{−19} J). All binding energies (BE) were referenced to the C 1s signal at 284.8 eV from carbon contamination of the samples to correct the charging effects. The area of the peaks was estimated by calculating the integral of each peak after smoothing and subtraction of an S-shaped background and fitting of the experimental curve to a mixture of Gaussian and Lorentzian lines (90G/10L). Quantification of the atomic fractions on the surface of CdS-*x* samples was obtained by integration of the peaks normalized with the corresponding sensitivity factors [41].

The UV–vis spectra of CdS-*x* samples were measured on a UV–vis–NIR Varian Cary 5000 spectrometer with double beam and double shutter synchronized electronically. The sources are deuterium (UV) and halogen quartz. The detectors were a multiplier and a refrigerated PbS detector for the NIR area. Band gap size was obtained from Tauc plots by plotting a tangent line over the slope of the UV–vis spectra and prolonging it to f(R) = 0 [42]. The wavelength value obtained was converted to given $E_{ph} = hc/\lambda$, where E_{ph} is the photon energy, h is the Planck constant, c the speed of light and λ the photon wavelength.

The photoluminescence (PL) and Raman spectra of CdS-*x* samples were carried out at room temperature using a WITec/ALPHA 300 AR confocal Raman system with excitation wavelength of 532 nm.

2.3. Photocatalytic activity tests

The photocatalytic hydrogen production on CdS-*x* samples was evaluated in a 230 mL closed Pyrex glass reactor working at room temperature and filled with Ar atmosphere (0.1 bar). A 50 mg of CdS powder was suspended in 150 mL of an aqueous solution containing 0.05 M Na₂S/0.02 M Na₂SO₃ as sacrificial electron donor agents [1,43]. Before irradiation, the reactor was purged with Ar for 1.5 h to ensure the complete air removal. A continuous magnetic stirrer was applied at the bottom of the reactor in order to keep the CdS particles under suspension during the photocatalytic test. The reactor was irradiated with a 150 W Xe arc lamp (ozone free, LOT Oriel GmbH & CO KG). Samples of 0.5 mL of the evolved gases were extracted from reactor periodically (every 1 h for a total reaction time of 5 h), and the amount of hydrogen was analysed by GC with TCD (Varian chromatograph Model Star 3400 CX) equipped with a 5A molecular sieve using Ar as carrier gas. Photoactivity results are presented in terms of rate of hydrogen production (μmol/h) during irradiation time (5 h).

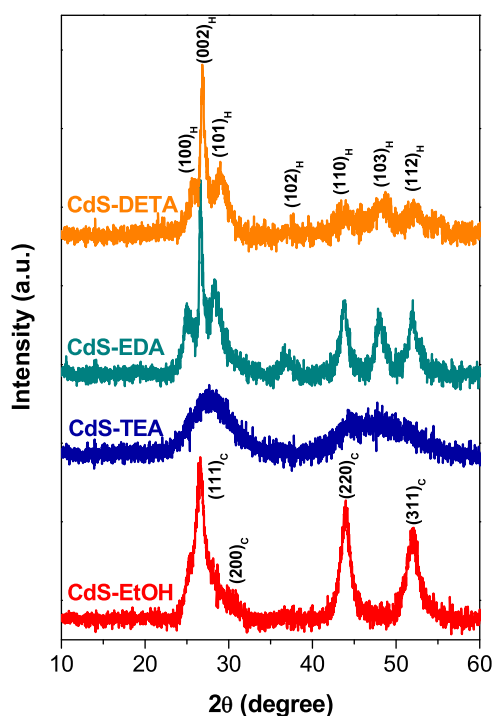


Fig. 1. XRD patterns of CdS-*x* samples synthesized by the solvothermal method using different solvents (120 °C and 12 h).

3. Results

3.1. Physicochemical characterization

3.1.2. X-ray diffraction (XRD)

The crystalline structure and phase composition of the prepared CdS-*x* samples were analysed by X-ray diffraction. Fig. 1 displays the diffraction patterns of the CdS-*x* samples showing that the solvents used in the solvothermal synthesis have an important effect on the crystal structure of the CdS particles [44]. Diffraction patterns of CdS-EDA and CdS-DETA samples can be indexed as (100), (002), (101), (102), (110), (103) and (112) planes of the hexagonal phase of the wurtzite CdS structure with P6₃mc space group and lattice parameters $a = 4.1360$ Å and $c = 6.7130$ Å (JCPDS 01-077-2306). In spite that no obvious peaks corresponding to the cubic phase were detected in the XRD patterns of CdS-EDA and CdS-DETA samples, the cubic/hexagonal phase content on these samples was approximately calculated from the integrated intensities of (110) and (103) planes [40,45,46]. The intensity of (103) plane is only assigned to the hexagonal phase of CdS, while the intensity of the (110) plane is the sum of both cubic and hexagonal contributions. The relative intensity ratio of the (110) and (103) planes for the CdS-DETA and CdS-EDA samples was 0.94. If we compare this value with the value reported for the standard XRD pattern of hexagonal CdS (0.96) it is clear that the crystalline structure of CdS-DETA and CdS-EDA samples are almost hexagonal. The strong and narrow (002) diffraction peaks observed in these samples were more intense than expected for the hexagonal phase. This indicates that the CdS crystals of CdS-DETA and CdS-EDA samples have a preferential orientation growth in the [001] direction (along the *c*-axis) with formation of 1D nanostructures [45,47]. For these samples, a quantitative estimation of the length and width of CdS crystallites was calculated by applying the Debye-Scherrer equation from the broadening of the (002) and (101) reflections respectively. The sample CdS-EDA presents a crystallite size of 22.0 nm length and 5.6 nm width, while the CdS-DETA sample shows lower val-

ues, 13.9 nm length and 4.4 nm width. The CdS-TEA sample shows broad diffraction peaks attributed to the incipient formation of (002), (110), (103) and (112) planes of a hexagonal phase of the CdS. These broad peaks indicate that the CdS-TEA sample consists of CdS particles of small size and poor crystallinity. Although it is difficult to distinguish the (103) and (110) peaks in the XRD pattern of the CdS-TEA sample, the ratio of the intensities of both peaks after careful deconvolution is about 0.94, suggesting the hexagonal crystal structure of this sample. The diffraction pattern of CdS-EtOH sample presents four reflection peaks at $2\theta = 26.5^\circ$, 30.7° , 44.0° and 52.0° characteristics of (111), (200), (220) and (311) reflections of the cubic phase of CdS (JCPDS 01-075-1546). Two additional weak diffraction peaks at $2\theta = 24.9^\circ$ and 28.3° are also detected that are attributed to the presence of a small contribution of CdS crystals with hexagonal phase.

3.1.2. FE-SEM and TEM analysis

The morphology of the CdS-*x* samples was investigated using field emission scanning electron microscopy (FE-SEM), transmission electron microscopy (TEM) and high-resolution transmission electron microscopy (HRTEM). Fig. 2 shows the FE-SEM images of the CdS-*x* samples which display different morphologies. As shown in Fig. 2a, the CdS-EtOH sample exhibits highly uniform and homogenous microspheres with diameters in the range 500–1200 nm. Fig. 2b reveals the solid nature of the microspheres and its granular surface. The morphology of the CdS-TEA sample shows (Fig. 2c and d) irregular agglomerates composed of globular particles not homogenous in size. In the case of the sample CdS-EDA (Fig. 2e and f) it is observed irregular clusters of CdS filaments heterogeneous in size (from 0.5 to 8 μm). Finally, the FE-SEM images of the CdS-DETA sample (Fig. 2g and h) show the surface formation of flower-like agglomerates with diameters around 1 μm.

The nanomorphology of CdS-*x* samples was analysed by TEM and HRTEM (Figs. 3–6). The TEM image of CdS-EtOH sample (Fig. 3a) shows spherical forms with diameter around 200 nm together with some less compact particles assembled from two-dimensional (2D) sheets. Fig. 3b and c display the HRTEM images of the CdS-EtOH sample taken from the labelled area in Fig. 3a. The lattice spacing of 0.336 nm in Fig. 3b is in accordance with the spacing of the (111) crystal plane of the cubic CdS. Moreover, Fig. 3c shows two lattice spacing of 0.316 and 0.336 nm that can be assigned to the (101) and (002) planes, respectively, of the hexagonal CdS. Therefore, the HRTEM images of the CdS-EtOH sample demonstrate, in agreement with previous XRD results, that this sample shows a crystal intergrowth of both phases.

TEM image of the CdS-TEA sample (Fig. 4a) reveals the presence of closely aggregated nanoparticles with irregular shape. HRTEM image of CdS-TEA nanoparticles (Fig. 4b) shows disordered structures with small crystalline domains in the size range 2–4 nm. The measured spacing of the crystallographic planes in nanoparticles are 0.358, 0.336 and 0.316 nm which correspond to the (100), (002) and (101) lattice spacing of hexagonal CdS planes respectively.

The CdS-EDA sample (Fig. 5) shows the formation of CdS nanosheets with incipient growth of small nanorods (Fig. 5a and b). HRTEM detail of nanorods in Fig. 5c shows the contact of the nanorods, with an average width range 8–10 nm, with small segregated crystals in the size range 2–4 nm (zone I Fig. 5c). The HRTEM image of nanorods (Fig. 5c) shows a lattice spacing of 0.336 nm which corresponds with the interplanar distance of the (002) planes of hexagonal CdS. The TEM image of CdS-DETA sample (Fig. 6a) presents morphology in form of sheets together with a small quantity of nanofibers (Fig. 6b). HRTEM detail in Fig. 6c also reveals the contact between sheets and small segregated crystals in the size range 2–4 nm (zone I Fig. 6c), similar to those observed in the CdS-EDA sample.

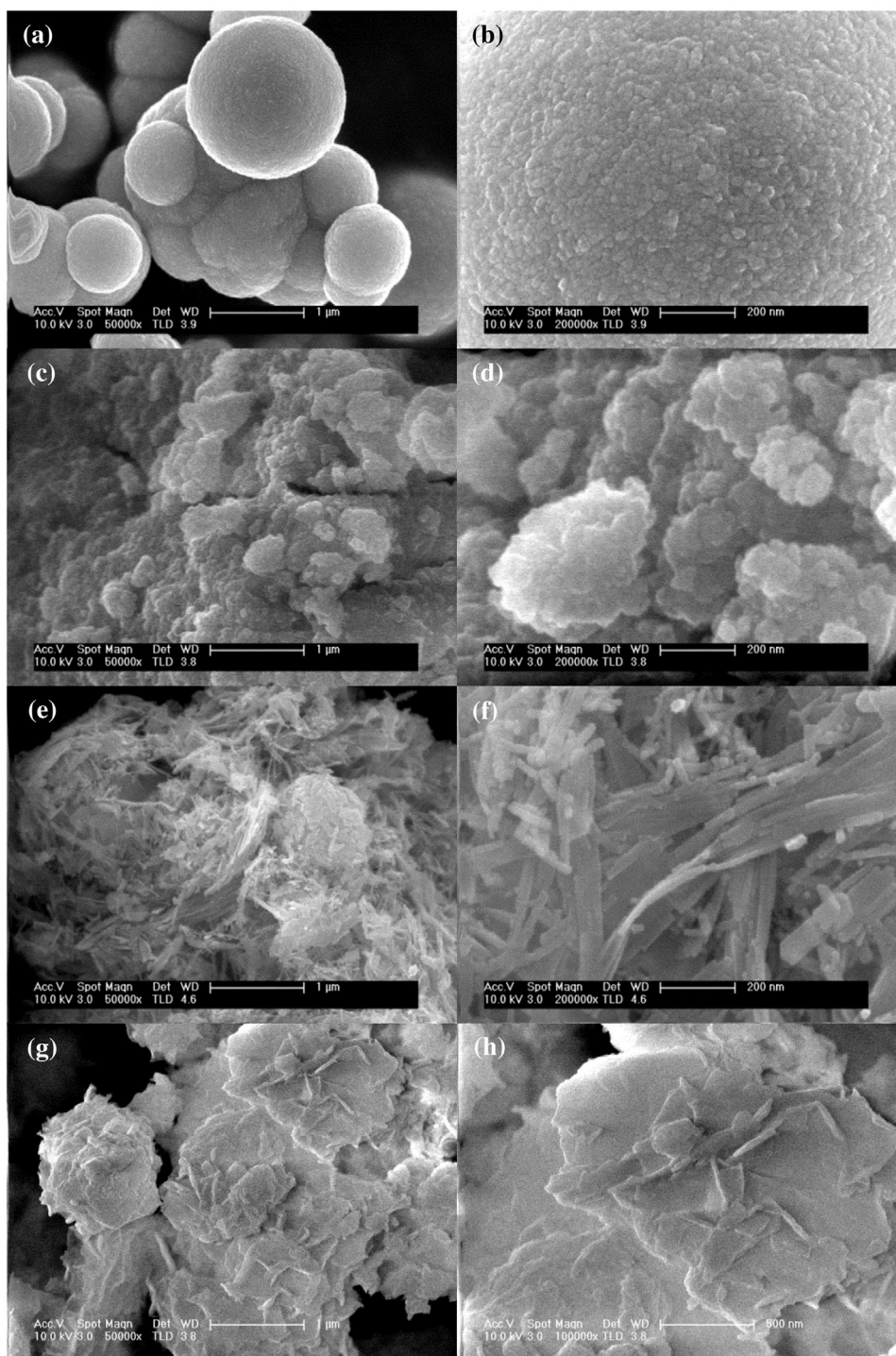


Fig. 2. FE-SEM images of CdS-*x* samples synthesized by the solvothermal method (120 °C and 12 h) with different solvents: CdS-EtOH (a and b), CdS-TEA (c and d), CdS-EDA (e and f) and CdS-DETA (g and h).

3.1.3. Raman analysis

Evaluation of structural properties of the CdS-*x* samples and changes in its crystallinity were studied by Raman spectroscopy. Amorphous or polycrystalline samples generally show a broad Raman bands while crystalline samples show sharp Raman bands [48–50]. The Raman vibrational modes of the hexagonal and cubic structures of CdS are very similar and from Raman spectroscopy is difficult to distinguish between these two structures [51,52]. Fig. 7 shows the room-temperature Raman spectra of CdS-*x* samples excited by 532 nm laser light. The first two peaks in the

Raman spectra of CdS-*x* samples correspond to the first-order (1LO) and second-order (2LO) longitudinal optical phonon modes of CdS [53–55]. Changes in intensity and position of Raman peaks were observed on CdS-*x* samples associated to their differences in crystallinity, size and morphology. For bulk CdS the fundamental 1LO and overtone 2LO modes are located at 305 and 605 cm^{-1} respectively [56–58]. It is known that crystalline size and morphology of CdS can downshift the Raman peaks as compared to the bulk CdS as result of the relaxation of the momentum conservation and the confinement of optical phonons in the nanometer-sized scale

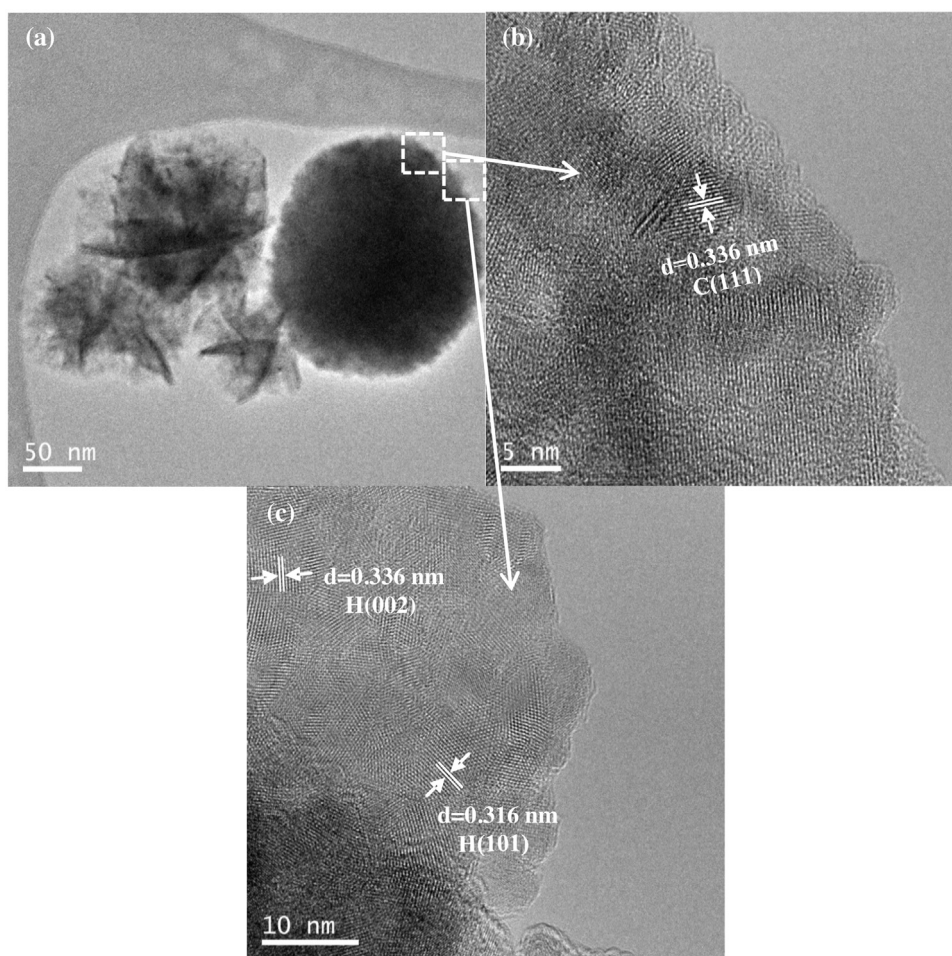


Fig. 3. TEM and HRTEM images of CdS-EtOH sample synthesized by the solvothermal method using ethanol as solvent (120 °C and 12 h).

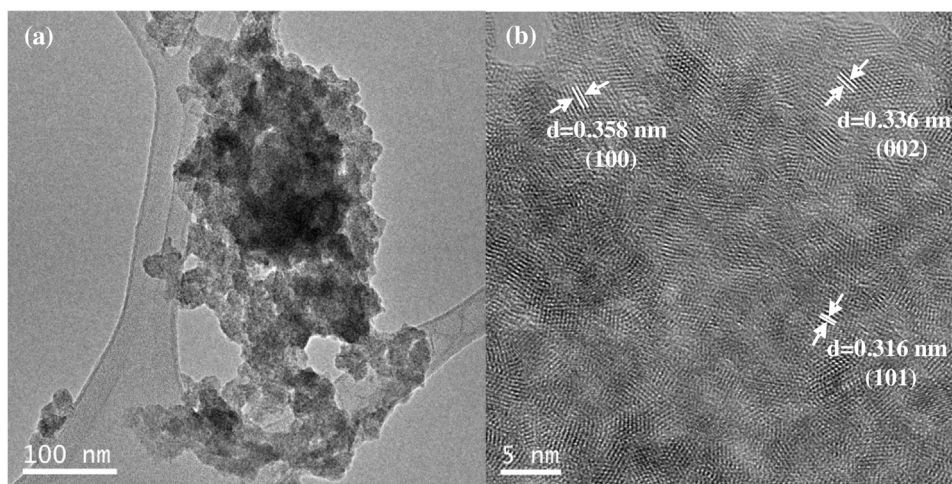


Fig. 4. TEM and HRTEM images of CdS-TEA sample synthesized by the solvothermal method using triethanolamine as solvent (120 °C and 12 h).

[59]. As CdS decreases in size, more red-shift and broadening of Raman peak are observed caused by the negative phonon dispersion curve [60]. The 1LO and 2LO peaks of CdS-DETA and CdS-EDA samples are located at 305 and 605 cm^{-1} respectively. The 1LO and 2LO Raman peaks of the CdS-TEA and CdS-EtOH samples redshift to 298 and 598 cm^{-1} respectively. The red-shift in the positions of the 1LO and 2LO modes observed in CdS-TEA and CdS-EtOH samples are in conformity with their lower crystalline size and their differ-

ent morphology: microspheres and nanoparticles, in comparison with the sheets and nanorods of CdS-DETA and CdS-EDA samples, respectively.

3.1.4. BET surface area and pore size distribution

The N_2 adsorption-desorption isotherms and the corresponding pore size distribution curves for the CdS-x samples are shown in Fig. 8a and b, respectively. All CdS-x isotherms (Fig. 8a) could be

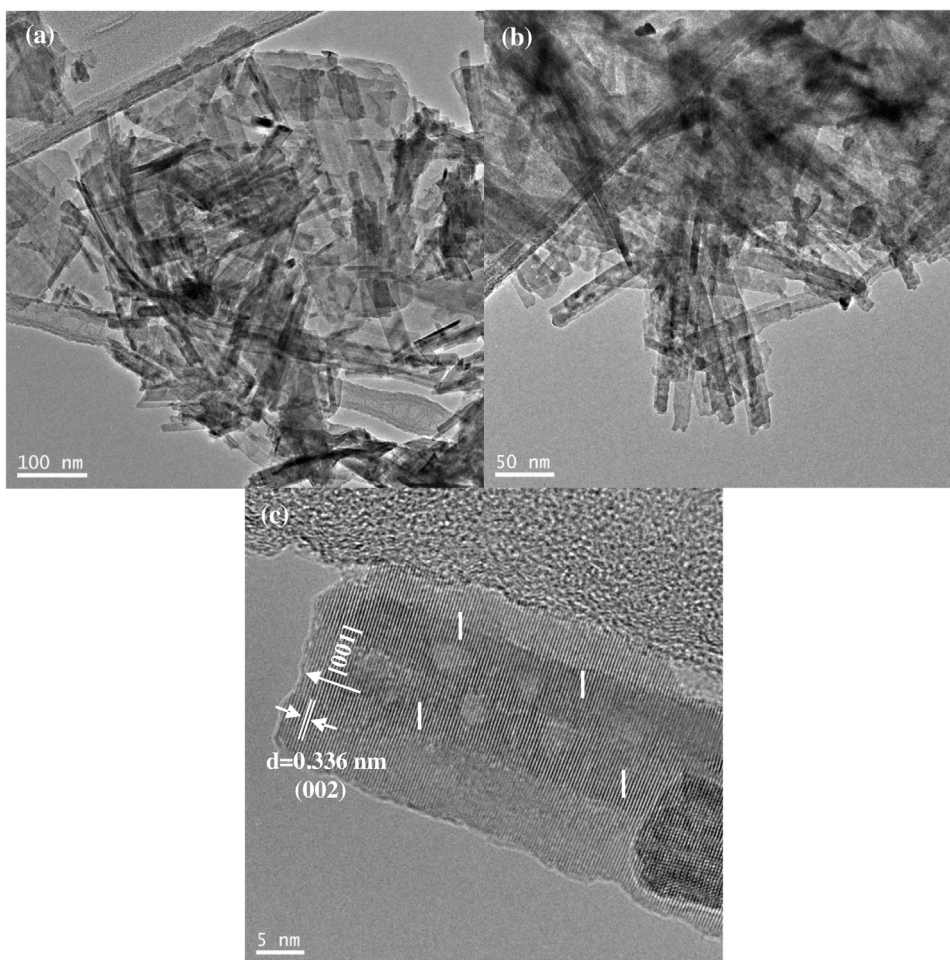


Fig. 5. TEM and HRTEM images of CdS-EDA sample synthesized by the solvothermal method using ethylenediamine as solvent (120 °C and 12 h).

Table 1

The specific surface area, pore volume and pore diameter of the CdS-*x* samples synthesized by the solvothermal method using different solvents (120 °C and 12 h).

Sample	BET (m ² /g)	APD ^a (nm)	PV ^a (cm ³ /g)
CdS-EtOH	17.0	3.8	0.02
CdS-TEA	12.4	10.9	0.03
CdS-EDA	67.2	16.7	0.40
CdS-DETA	51.1	14.6	0.21

^a APD: average pore diameter; PV: pore volume.

assigned to type IV (characteristic of mesoporous materials, IUPAC classification) according to their shape [61]. The isotherms of all CdS-*x* samples exhibit H3 hysteresis loop associated to the presence of ink-bottle pores with narrow necks and wider bodies [62]. The average pore size, pore volume and BET surface area of CdS-*x* samples derived from N₂ adsorption-desorption isotherms are listed in Table 1. It can be seen that the specific surface area developed by CdS-*x* samples is affected by the solvent used in the synthesis. The pore size distribution plot of CdS-*x* samples (Fig. 8b) shows two different levels of pores. The CdS-EtOH and CdS-TEA samples present pore diameters lower than 10 nm, with maximum pore diameters around 3.4–3.8 nm for the CdS-EtOH sample and 3.3–4.7 nm in the case of the CdS-TEA sample. The CdS-EDA and CdS-DETA samples exhibit a wide pore size distribution including mesopores, around 3.6–3.7 nm, and macropores with maximum pore diameter around 39 nm (CdS-DETA) and 42 nm (CdS-EDA) [34]. It could be assumed that the porous structures of the CdS-*x* samples are formed by the agglomeration of primary CdS particles. The higher aggregation of

Table 2

XPS binding energies of core electrons of the CdS-*x* samples synthesized by the solvothermal method using different solvents (120 °C and 12 h).

Sample	Cd 3d _{5/2} (eV)	S 2p _{3/2} (eV)	N 1s (eV)	O 1s (eV)
CdS-EtOH	405.0	161.4	–	531.6
CdS-TEA	405.2	161.4	399.8	531.6
CdS-EDA	405.0	161.4	399.9	531.6
CdS-DETA	405.1	161.4	399.9	531.6

primary CdS nanoparticles observed by TEM on CdS-EtOH and CdS-TEA samples (Fig. 3–4) is in line with the low surface area and small mesopores observed on these samples. On the contrary, the wide pore distribution and high surface area achieved on CdS-EDA sample fit well with the lower aggregation of CdS particles observed in their TEM images (Fig. 5). The CdS-DETA sample shows a slight reduction in the surface area respect to that developed on CdS-EDA as consequence of its higher aggregation degree (Fig. 6). Therefore the CdS-*x* samples with less aggregation of primary particles, CdS-EDA and CdS-DETA, develop a more extended porous structure that could be useful in photocatalytic hydrogen production since it could provide efficient transport pathways to the interior void space [63].

3.1.5. XPS analysis

The chemical species and their relative concentration on the surface of the CdS-*x* samples were analysed by XPS. The Cd 3d_{5/2}, S 2p, N 1s and O 1s core-levels for all CdS-*x* samples are recorded and the binding energies are collected in Table 2. The CdS-*x* samples shows a Cd 3d_{5/2} level (Fig. 9a) with binding energies at 405.0–405.2 eV.

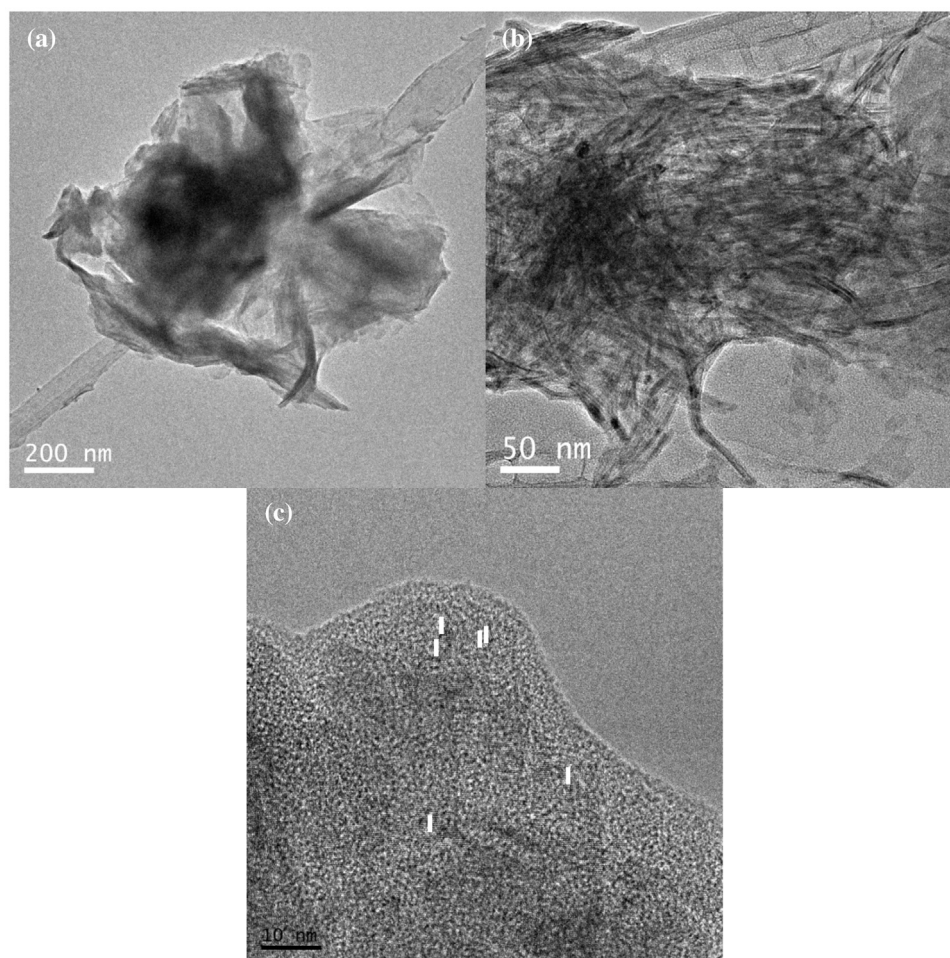


Fig. 6. TEM and HRTEM images of CdS-DETA sample synthesized by the solvothermal method using diethylenetriamine as solvent (120 °C and 12 h).

Table 3

XPS surface composition (atomic percentage) of the CdS-*x* samples synthesized by the solvothermal method using different solvents (120 °C and 12 h).

Sample	Cd (%)	S (%)	N (%)	O (%)	Cd/S	Cd/(S + O)
CdS-EtOH	49.6	38.2	0.0	12.2	1.29	0.98
CdS-TEA	41.0	35.5	0.5	23.0	1.15	0.70
CdS-EDA	45.4	38.2	8.1	8.3	1.19	0.99
CdS-DETA	41.4	30.2	13.3	15.1	1.37	0.91

The binding energies are close to that reported for CdS [64]. The S $2p_{3/2}$ level of all CdS-*x* samples (Fig. 9b) shows a symmetric peak close to 161.4 eV, characteristic of S^{2-} species. The XPS spectra of the O 1s level (Fig. 9c) show a main contribution at 531.6 eV indicative of the presence of oxygen coordinated with sulfate species. The presence of sulfate species at surface level is derived from the surface oxidation of CdS by oxygen from air favoured under ambient light irradiation [65]. The CdS-*x* samples prepared using solvents with amino groups show signals in the N 1s level (not shown here) indicative of the existence of some solvent remnants on the surface of CdS-*x* samples.

The surface concentrations of Cd, S, N and O calculated from XPS intensities are listed in Table 3. In all CdS-*x* samples it is observed a metal/sulfur surface ratio higher than unity indicative of an impoverishment in sulfur as consequence of the presence of nitrogen (from solvents) and/or oxygen coordinated with Cd at the surface. Nitrogen from solvents was observed in samples prepared with amines and its concentration is particularly important in the case of the samples CdS-DETA and CdS-EDA. In these samples, the impoverishment in sulfur at surface level could be also related with the possibility of sulfur vacancies caused by the amine solvents at surface, because according to previous studies in the literature [66,67] the amine ligands can act as a cation sequestering binding to the Cd^{2+} ions on the CdS surface and creating sulfur vacancies.

The concentration of oxygen at surface was also significant in all CdS-*x* samples. The oxygen concentration on samples decreases following the sequence: CdS-TEA > CdS-DETA > CdS-EtOH > CdS-EDA. This sequence is indicative of differences in the surface oxidation of CdS by oxygen from air. Higher surface oxidation was observed on CdS-TEA sample and it probably arises from its amorphous character and low particle size since these characteristics contribute to increase the probability of surface oxidation [68]. Lower surface oxidation was observed on CdS-EtOH, CdS-DETA and CdS-EDA samples as consequence of their higher crystallinity and size. In the case of the CdS-DETA and CdS-EDA samples, the coordination of solvent molecules on the CdS surface could also passivate the surface preventing the absorption of oxygen and diminishing by this way the oxidation by air.

erishment in sulfur at surface level could be also related with the possibility of sulfur vacancies caused by the amine solvents at surface, because according to previous studies in the literature [66,67] the amine ligands can act as a cation sequestering binding to the Cd^{2+} ions on the CdS surface and creating sulfur vacancies.

3.1.6. Photoluminescence analysis

Fig. 10 shows the photoluminescence (PL) spectra of CdS-*x* samples measured at room temperature with excitation wavelength of 532 nm. The PL behaviour of CdS nanostructures has been studied intensively [69–72] and according to these studies, CdS nanostructures generally have two PL emissions: band-edge emission (at 420–500 nm) [71–74] and surface-defect emission (at

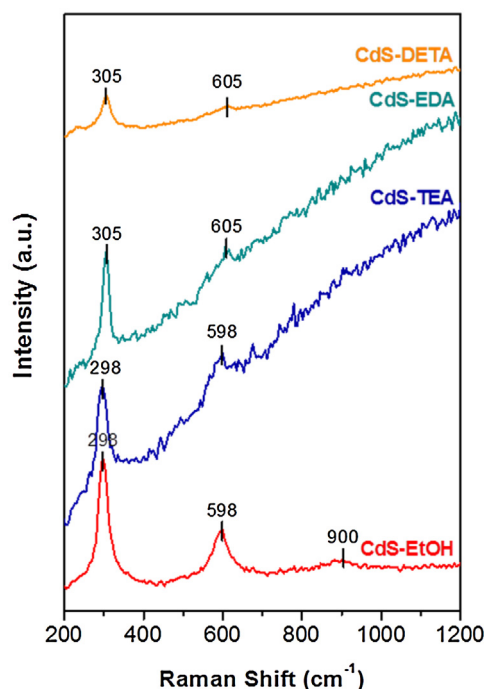


Fig. 7. Raman spectra of CdS-*x* samples synthesized by the solvothermal method using different solvents (120 °C and 12 h).

530–680 nm) caused by surface states such as sulfur vacancies or/and sulfur dangling bonds [69,70,75].

The PL spectra of CdS-*x* samples exhibit a broad PL emission band with three emission peaks at 580, 607 and 627 nm. The emission at 580 nm is attributable to the recombination of an electron trapped in a sulfur vacancy with a hole in the valence band of CdS [69,70]. The next emission at 607 nm is due to deep level or trap states [76–78], and the emission tail at 627 nm is attributed to defects in the intergranular regions [78–80]. The sample CdS-EtOH shows the lowest PL intensity associated with a low rate of recombination processes (low density of surface defects). On the contrary, the CdS-DETA sample exhibits the highest PL intensity related to a shorter lifetime of photogenerated electron-hole pairs as consequence of its high rate of recombination. The CdS-EDA and CdS-TEA samples show similar PL intensity associated with sulfur vacancies at 580 nm while the CdS-TEA increases the PL intensity at 627 nm associated with defects in the intergranular regions. By comparing the crystallinity of the CdS-*x* samples with the PL spectra (Fig. 10) no direct correlation was found indicating that PL spectra of CdS-*x* samples are derived from defects (sulfur vacancies and intergranular defects) not evaluated from XRD analyses.

3.1.7. UV-vis spectra

Fig. 11a shows the UV-vis absorption spectra of the CdS-*x* samples. The CdS-*x* samples showed different absorption edge whose definition and position are dependent on the solvent used in the solvothermal synthesis. The definition and narrowing of the absorption edge increase following this sequence CdS-DETA < CdS-TEA < CdS-EDA < CdS-EtOH. It has been shown [81] that in nanostructures, the rise in the structural defects and strain lead to a broadening of the optical absorption edge. Therefore, the sequence in the definition of the absorption edge observed on CdS-*x* samples may be related with a decrease in the structural defects and strain of CdS following this sequence. Characterization by photoluminescence of CdS-*x* samples (Fig. 10) agrees with the sequence of structural defects derived from the differences in the UV-vis absorption edges. The absorbance intensity at a wavelength

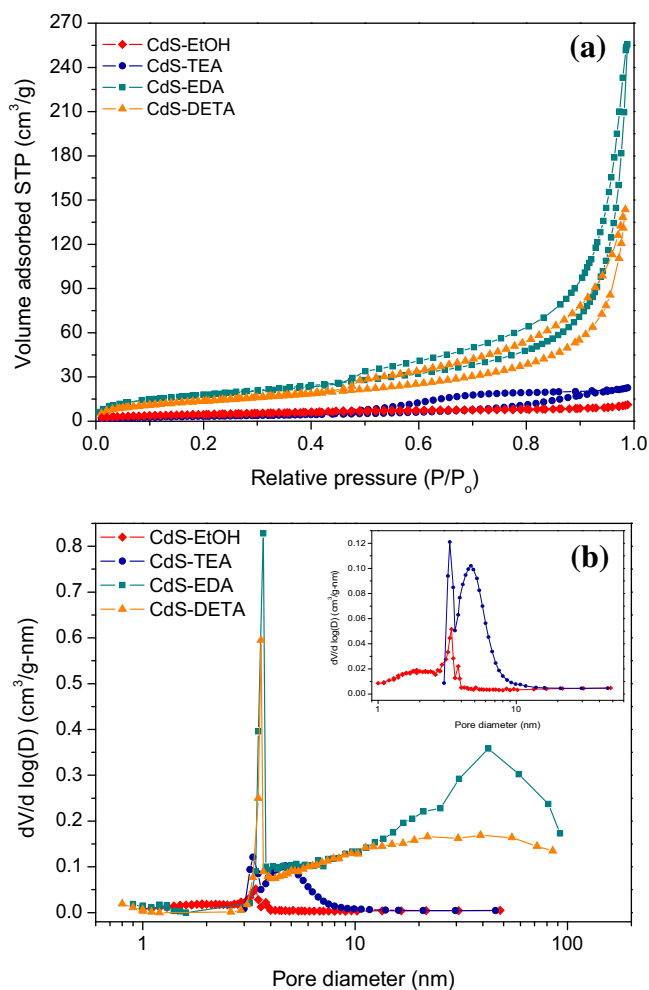


Fig. 8. N₂ adsorption-desorption isotherms (a) and pore-size distribution curves (b) of CdS-*x* samples synthesized by the solvothermal method using different solvents (120 °C and 12 h).

Table 4

Band gap energy of the CdS-*x* samples synthesized by the solvothermal method using different solvents (120 °C and 12 h).

Sample	Band Gap (eV)
CdS-EtOH	2.40
CdS-TEA	2.65
CdS-EDA	2.50
CdS-DETA	2.93

of less than 550 nm also shows differences between the CdS-*x* samples. Variations in size of the CdS nanostructures may contribute to the observed changes in the absorbance intensity because small particles favour deep penetration of the radiation into the particles.

The band gap size for each CdS-*x* sample, calculated from Tauc plots (Fig. 11b), are listed in Table 4. Compared to the band gap of crystalline CdS in hexagonal phase (2.40 eV), all samples, except the CdS-EtOH, show blue shift. The absorption spectra of CdS-EDA and CdS-DETA samples also show a well-defined excitonic peak at 370 nm. This excitonic peak is result of the very strong quantum confinement effect (SQE) due to the presence of small CdS crystalline nanostructures of diameter lower than the CdS exciton Bohr radius (2.5 nm) [82]. It is possible to deduce the size of these small CdS nanostructures using the Brus formula from the absorption position of the exciton peak [83]. According to this formula the calculated size of these small CdS nanostructures was 2.2 nm close to the diameter of the randomly arranged crystal lattices observed

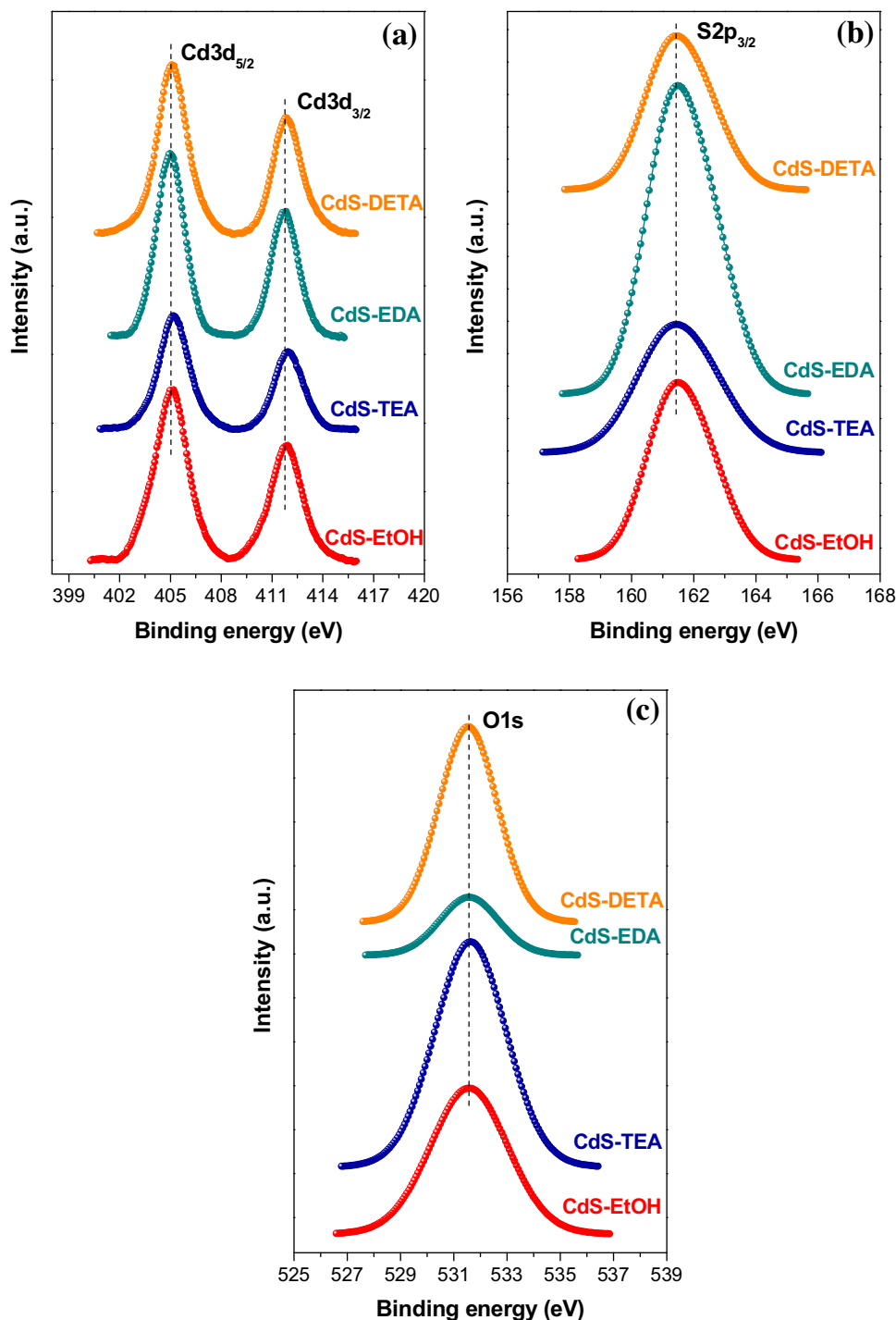


Fig. 9. Cd 3d_{5/2} (a), S 2p_{3/2} (b) and O 1s (c) XPS levels of CdS-x samples synthesized by the solvothermal method using different solvents (120 °C and 12 h).

by TEM on CdS-EDA (zone I in Fig. 5c) and CdS-DETA samples (zone I in Fig. 6c).

3.1.8. Photocatalytic activity measurements

Photocatalytic hydrogen production of the different CdS-x samples from aqueous solution containing Na₂S + Na₂SO₃ as sacrificial electron donor agents were measured under irradiation with a 150 W Xe arc lamp. Fig. 12 shows the hydrogen evolution rate on the CdS-x samples. Blank experiments showed no appreciable H₂ evolution in the absence of either a photocatalyst or irradiation, implying that H₂ was produced *via* photocat-

alytic reactions. As shown in Fig. 12, the photoactivity on CdS-x samples displays important differences in the rate of hydrogen production. The sample CdS-EDA showed the highest hydrogen production rate (24.94 μmol h⁻¹) followed by the CdS-DETA sample (19.40 μmol h⁻¹). The CdS-TEA and CdS-EtOH samples show photocatalytic activity values much lower. This indicates that changes in the morphology and structure of CdS associated to the different solvent used in the solvothermal synthesis play an important role in the photocatalytic activity towards hydrogen production. In order to evaluate the photostability of the CdS-x samples, the stability of the CdS-EDA sample was studied by analysing

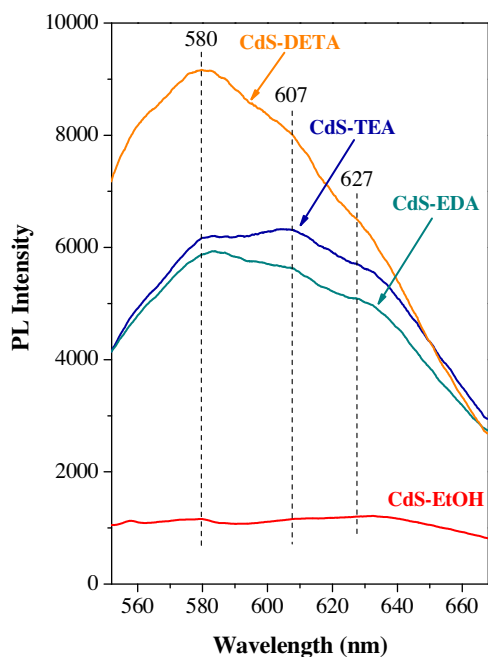


Fig. 10. PL spectra of CdS-*x* samples synthesized by the solvothermal method using different solvents (120 °C and 12 h).

their photocatalytic behaviour in light on/light off cycles. As a result, no signs of deactivation were observed after 5 cycles. To corroborate the absence of photocorrosion of CdS under photocatalytic testing we also analysed by XPS some samples before and after the photocatalytic tests. From these analyses we did not find any evidence of photocorrosion in any of the analysed samples indicating the stabilization of the photocatalyst surfaces by the presence of excess S^{2-}/SO_3^{2-} ions in the reaction solution.

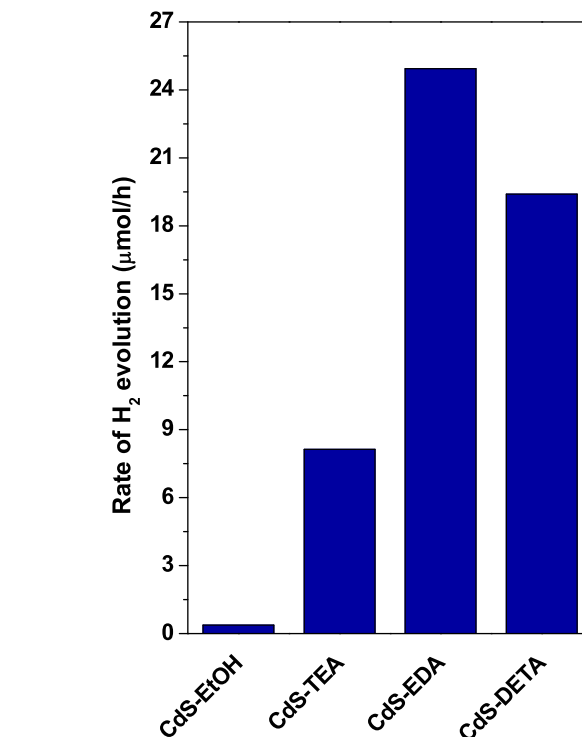
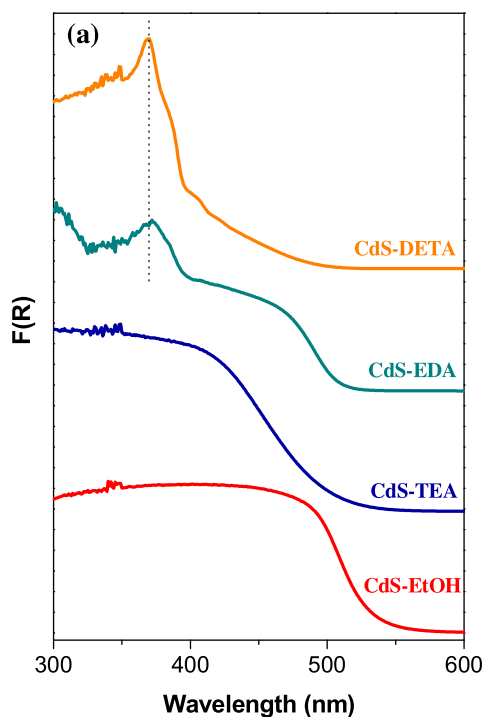


Fig. 12. Hydrogen evolution rate over CdS-*x* photocatalysts from aqueous solution containing $Na_2S + Na_2SO_3$ sacrificial reagents under visible light irradiation (0.05 g, 150 mL (0.05 M Na_2S /0.02 M Na_2SO_3), 150 W Xe lamp, $t = 5$ h).

4. Discussion

4.1. Influence of solvent on the structure and morphology of CdS

The changes in the morphology and structure of the CdS-*x* samples prepared with different solvents are derived from the dif-

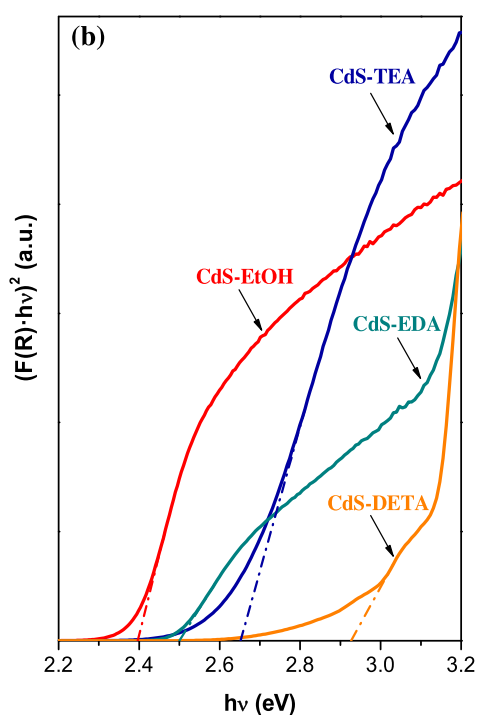


Fig. 11. UV-vis spectra (a) and the Tauc plot for band gap determination (b) of CdS-*x* samples synthesized by the solvothermal method using different solvents (120 °C and 12 h).

ferences in the coordination and dielectric constant of solvents which control the molecular mechanism for the CdS growth. It should be noted that the morphology of CdS is intimately related with the growth direction of nanocrystals that comprise it.

The solvents EDA and DETA contain nitrogen atoms that can be coordinated to superficial Cd atoms in the (100) and (010) faces controlling their relative growth. While the EDA molecule prefers to be vertically adsorbed on the (100) and (010) faces, in the case of the DETA molecule, the horizontal and vertical adsorptions on the (100) and (010) faces are possible [31,45]. The EDA molecule can limit the growth of (100) and (010) faces because the distance between adjacent three-coordination N atoms in the EDA molecule is equal to that between adjacent Cd atoms in (100) and (010) faces, enhancing its interaction with CdS surface. As a result, the CdS-EDA sample presents rod-like morphology. In the case of the DETA solvent, the horizontal and vertical adsorption on (100) and (010) faces are weaker than the horizontal adsorption of EDA molecule. This fact causes that the growth in the (100) and (010) faces in DETA solvent are faster than in EDA solvent leading to the observed morphology of sheets. For the CdS sample prepared with TEA as solvent, the presence of oxygen in its atomic chain introduces O atoms in the lattice of CdS changing the crystal structure. Hence, the CdS-TEA sample presents irregular nanoparticles as morphology. As indicated previously, the growth direction of crystals determines its morphology. It should be noted that if the rate of growth in all directions is slow, the morphology of CdS crystals will be spherical due to the minimum surface energy effect. This effect is prevalent in the CdS sample synthesized with EtOH as solvent because the alcohol does not coordinate with surface Cd atoms being not able to modify the directional growth rate as EDA or DETA molecules do.

Another aspect to be considered is the dielectric constant of solvents because it influences on the solubility of CdS and therefore on the crystal growth and crystallinity. The dielectric constants of ethanol, triethanolamine, ethylenediamine and diethylenetriamine are 24.3, 28.9, 13.82 and 12.0 respectively. It is established that the free energy difference between cubic and hexagonal structures for CdS is small [84]. Thus, solvents with low dielectric constant may minimize the free energy difference between the hexagonal and cubic phases, and thus favour the formation of hexagonal phase CdS [85]. Decreasing the dielectric constant of the solvent (DETA and EDA) also implies lower solubility of CdS that means higher supersaturation degree with higher nuclei, an improved supply rate, faster crystal growth and therefore higher crystallinity. This fact is in good agreement with the XRD patterns observed for the CdS-*x* samples synthesized (Fig. 1). The use of solvents with high dielectric constant (EtOH and TEA) leads to crystal growth in equilibrium state forming spherical and particle-like structures.

Taking into account all the above aspects, Fig. 13 summarizes a schematic diagram illustrating the growth of different CdS structures in the presence of the studied solvents. As shown in Fig. 13, a small part of 2D sheets were transformed into 1D nanostructures according to the mechanism of formation of nanorods by rolling and breaking of sheets previously established in the literature [29,37,47,58,86].

4.2. Dependency of photoactivity on the structure and morphology of CdS

The physicochemical characterization of the CdS-*x* samples has shown that solvents induce changes in the morphology, structure and composition of the particles of CdS obtained. These parameters affect the absorption of photons and the generation, separation, migration and transfer of the photogenerated charge carriers (e^-/h^+) [9,87] and, therefore the final photocatalytic behaviour of

the CdS-*x* samples (Fig. 12). The absorption of photons and the photogeneration of charge carriers (e^-/h^+) are related to the UV–vis absorption spectra of the CdS-*x* samples (Fig. 11). The comparison of hydrogen production on CdS-*x* samples (Fig. 12) with their photooptical properties (Fig. 11 and Table 4) indicates absence of correlation between both parameters. Therefore, the differences in the photoactivity of the CdS-*x* samples should be related with other characteristics such as the separation and migration of photogenerated charge carriers (e^-/h^+). The efficient transport of photoexcited carriers is determined by the crystal size, the crystalline structure, the nature and number of structural defects and the surface properties of photocatalysts. As a general rule, high crystallinity and low particle size have a positive effect on photoactivity of CdS [9,29,88]. The XRD patterns of CdS-*x* samples (Fig. 1) shows differences in crystal phase, crystallinity and size. The CdS-EtOH sample crystallizes in cubic phase with small contribution of hexagonal phase. This fact justify the low photoactivity observed for this sample (Fig. 12) because CdS crystals with hexagonal structure are known to be much more efficient in hydrogen production than counterparts with cubic crystal structure [89]. The formation of internal electric field in hexagonal CdS is beneficial for the efficient separation and diffusion of photogenerated charge carriers. Moreover, the effective mass of photogenerated charge carriers of hexagonal CdS is smaller than those of cubic CdS, implying faster migration of photogenerated charge carriers [84]. The CdS-EDA and CdS-DETA samples present similar hexagonal crystallinity and much higher crystallinity than that observed for the CdS-TEA sample which shows poor crystalline growth. By comparing the crystallinity of the CdS-EDA, CdS-DETA and CdS-TEA samples with their photocatalytic H_2 -production rate (Fig. 12), a direct correlation was found between these two parameters. This result is in line with other studies such as Yu et al. [31] which showed that photoactivity of CdS prepared by solvothermal synthesis with different solvents correlated with the crystallinity of the samples. The density of surface defects could also modify the photocatalytic activity of CdS-*x* samples because they can serve as electron traps and recombination centres for electrons and holes [45,88,90]. Low rate of recombination results in the improvement of the photocatalytic H_2 production. Analyzing the surface defects on CdS-*x* samples from PL spectra (Fig. 10) it was observed that the density of surface defects decreases in the order CdS-DETA > CdS-TEA > CdS-EDA and therefore the influence of the charges recombination on the overall H_2 production should decrease in the same order.

Hierarchy at nanometer scale has also been identified as a factor to be analysed in order to elucidate the origin of the changes in the photoactivity of the CdS-*x* samples [91]. Taking this fact into account, the UV–vis absorption spectra of the CdS-*x* samples synthesized with ethylenediamine and diethylenetriamine as solvents (Fig. 11) shows the presence of small CdS nanocrystals with strong quantum confinement effect (CdS-SQE, zone I in Figs. 5 c and 6 c, and exciton peaks at 370 nm in Fig. 11). CdS nanostructures showing strong quantum confinement effect (SQE) have been reported to improve the photoactivity when combines with other semiconductors such as TiO_2 [92], ZnO [93], graphene [94,95] or C_3N_4 [96] because the CdS-SQE nanostructures significantly enhance the surface amplitude of electrons and holes facilitating interfacial reactions. Therefore, the high hydrogen production rates obtained over CdS-EDA and CdS-DETA samples could be related with the presence of the CdS-SQE on these samples. In addition to the existence of the CdS-SQE nanocrystals, the hierarchically assembling of these nanocrystals with CdS in form of nanorods could also plays an important role in the photoactivity since the samples prepared with EDA and DETA showed similar CdS-SQE nanocrystals (same excitonic peak at 370 nm in Fig. 11), while their photoactivity differs considerably (Fig. 12). Nanorod structures having width close to the exciton Bohr radius, as the CdS-EDA sample, have the ability

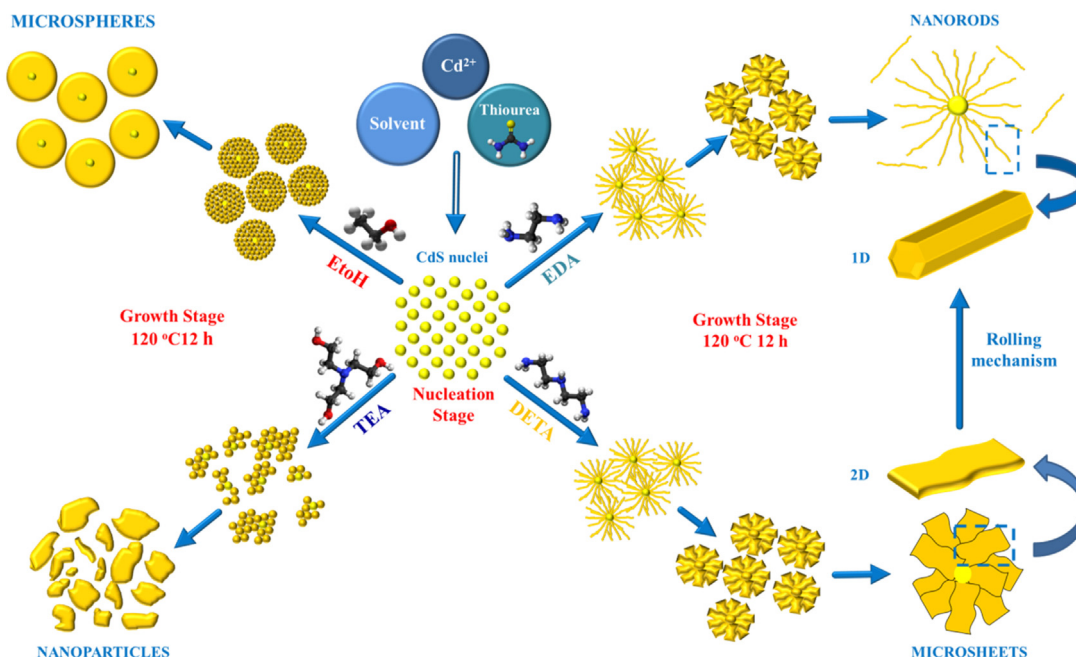


Fig. 13. Schematic diagram showing the formation of CdS structures with various morphologies by the solvothermal method using different solvents (120 °C and 12 h).

to delocalize charge carriers (e^-/h^+) along the length of the nanostructure but confined in the radial direction slowing down their recombination and facilitating a more efficient charge separation than others nanostructures [97,98]. Therefore, the better photocatalytic H_2 -production rate showed by the CdS-EDA sample could be related with the hierarchically integration of CdS-SQE nanocrystals with nanorods in line with other hierarchical CdS self-assembled nanostructures previously published in the literature [63] that facilitate the separation of photo-generated electron-hole pairs. The effect of amine ligands on surface of CdS detected on CdS-EDA and CdS-DETA could also be responsible of the high photoactivity observed on these samples because amines linked to the surface Cd^{2+} ions creates surface states that promotes the transference of the photogenerated electrons to the protons to produce hydrogen [45].

The surface area influences on the efficiency of charge carriers use (in surface reduction/oxidation reactions) and in consequence is also a parameter to analyze in the photoactivity behaviour of CdS-x samples [88,99]. Fig. 14 represents the rate of hydrogen production normalized per surface area in order to extract the possible influence of surface/bulk structural changes upon the photoactivity of CdS-x samples.

As shown in Fig. 14, the CdS-EDA and CdS-DETA samples show similar surface-normalized hydrogen production rates. This fact indicates that the photoactivity of these samples is mainly related to the changes in the surface area more than the changes in the crystallinity and size observed on these samples. As shown in Fig. 14, the sample CdS-TEA presents a sharp increase in the rate of hydrogen production normalized per surface area with respect to the values achieved on the CdS-EDA and CdS-DETA samples. This fact indicates that for the CdS-TEA sample the surface characteristics prevails against the lower recombination of e^-/h^+ associated to the higher crystalline degree of the CdS structures obtained in the case of CdS-EDA and CdS-DETA samples. Changes at surface level in the CdS-TEA sample may play a role in its high normalized photoactivity. In this sense, the significant presence of oxygenated species detected in the surface of the CdS-TEA sample (Table 3 XPS) may also play a role in the improvement of activity observed in this

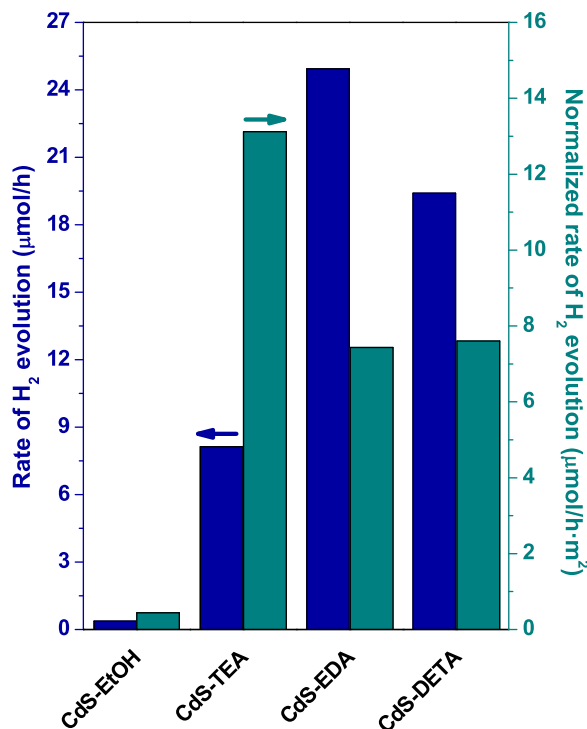


Fig. 14. Comparison of rate of hydrogen production normalized per surface area and rate of hydrogen production over CdS-x photocatalysts synthesized by the solvothermal method (120 °C and 12 h) using different solvents.

sample. The presence of oxygen in surface in the form of sulfates may enhance the adsorption of H_2O and $\text{S}^{2-}/\text{SO}_3^{2-}$ on photocatalyst surface improving its interaction with the generate e^-/h^+ carriers. Nevertheless this assumption needs to be corroborated in a further research.

5. Conclusions

The solvents used in the solvothermal synthesis play an important role in the growth, structure and crystallinity of CdS. Nanostructures of CdS with the highest crystallinity and surface area in the form of nanorods were obtained using ethylenediamine as solvent whereas sheets were produced in the case of diethylenetriamine solvent. The use of triethanolamine produces irregular particles of poorly crystalline hexagonal CdS whereas in the case of ethanol leads to the formation of spherical cubic CdS crystals. The photoactivity results for hydrogen production show that samples of CdS with hexagonal crystallinity prepared with ethylenediamine and diethylenetriamine achieve the higher photoactivity values, whereas CdS samples prepared using ethanol and triethanolamine show the lower photoactivity as consequence of their poor crystallinity and formation of cubic phase respectively. The improvement in photoactivity could be related with the presence of small CdS nanocrystals with strong quantum confinement effect on samples prepared using ethylenediamine and diethylenetriamine. In spite of the low H_2 production rate obtained on the sample prepared using triethanolamine solvent, this sample shows the higher rate of H_2 production normalized per surface area that could be derived from the presence of oxygen in surface in the form of the sulfates which may enhance the adsorption of H_2O and S^{2-}/SO_3^{2-} on photocatalyst surface.

Acknowledgements

The present work was performed within the research programs supported by the Secretaría de Estado de Investigación, Desarrollo e Innovación and CAM (Spain) under projects CTQ2013-48669-P and S2013/MAE-2882, respectively. F. Vaquero would like to acknowledge the Secretaría de Estado de Investigación, Desarrollo e Innovación for the FPI research grant.

References

- [1] I. Tsuji, H. Kato, H. Kobayashi, A. Kudo, Photocatalytic H_2 evolution reaction from aqueous solutions over band structure-controlled $(AgIn)_xZn_{2(1-x)}S_2$ solid solution photocatalysts with visible-light response and their surface nanostructures, *J. Am. Chem. Soc.* 126 (2004) 13406–13413.
- [2] K. Maeda, T. Takata, M. Hara, N. Saito, Y. Inoue, H. Kobayashi, K. Domen, $GaN:ZnO$ solid solution as a photocatalyst for visible-light-driven overall water splitting, *J. Am. Chem. Soc.* 127 (2005) 8286–8287.
- [3] F.E. Osterloh, Inorganic materials as catalysts for photochemical splitting of water, *Chem. Mater.* 20 (2007) 35–54.
- [4] F. del Valle, A. Ishikawa, K. Domen, J.A. Villoria de la Mano, M.C. Sánchez-Sánchez, I.D. González, S. Herreras, N. Mota, M.E. Rivas, M.C. Álvarez Galván, J.L.G. Fierro, R.M. Navarro, Influence of Zn concentration in the activity of $Cd_{1-x}Zn_xS$ solid solutions for water splitting under visible light, *Catal. Today* 143 (2009) 51–56.
- [5] A. Kasahara, K. Nukumizu, G. Hitoki, T. Takata, J.N. Kondo, M. Hara, H. Kobayashi, K. Domen, Photoreactions on $LaTiO_2N$ under visible light irradiation, *J. Phys. Chem. A* 106 (2002) 6750–6753.
- [6] H. Kato, K. Asakura, A. Kudo, Highly efficient water splitting into H_2 and O_2 over lanthanum-doped $NaTaO_3$ photocatalysts with high crystallinity and surface nanostructure, *J. Am. Chem. Soc.* 125 (2003) 3082–3089.
- [7] A. Kudo, K. Omori, H. Kato, A novel aqueous process for preparation of crystal form-controlled and highly crystalline $BiVO_4$ powder from layered vanadates at room temperature and its photocatalytic and photophysical properties, *J. Am. Chem. Soc.* 121 (1999) 11459–11467.
- [8] X. Chen, S. Shen, L. Guo, S.S. Mao, Semiconductor-based photocatalytic hydrogen generation, *Chem. Rev.* 110 (2010) 6503–6570.
- [9] R.M. NavarroYerga, M.C. Álvarez-Galván, F. Vaquero, J. Arenales, J.L.G. Fierro, Chapter 3 – hydrogen production from water splitting using photo-Semiconductor catalysts, in: L.M. Gandía, G. Arzamendi, P.M. Diéguez (Eds.), *Renewable Hydrogen Technologies*, Elsevier, Amsterdam, 2013, pp. 43–61.
- [10] M. Matsumura, Y. Saho, H. Tsubomura, Photocatalytic hydrogen production from solutions of sulfite using platinized cadmium sulfide powder, *J. Phys. Chem.* 87 (1983) 3807–3808.
- [11] M.R. Hoffmann, S.T. Martin, W. Choi, D.W. Bahnemann, Environmental applications of semiconductor photocatalysis, *Chem. Rev.* 95 (1995) 69–96.
- [12] A.A. Ismail, D.W. Bahnemann, Photochemical splitting of water for hydrogen production by photocatalysis: a review, *Sol. Energy Mater. Sol. Cells* 128 (2014) 85–101.
- [13] J.F. Reber, M. Rusek, Photochemical hydrogen production with platinized suspensions of cadmium sulfide and cadmium zinc sulfide modified by silver sulfide, *J. Phys. Chem.* 90 (1986) 824–834.
- [14] M. Ashokkumar, An overview on semiconductor particulate systems for photoproduction of hydrogen, *Int. J. Hydrogen Energy* 23 (1998) 427–438.
- [15] B. Pal, T. Torimoto, K. Iwasaki, T. Shibayama, H. Takahashi, B. Ohtani, Size and structure-dependent photocatalytic activity of jingle-bell-shaped silica-coated cadmium sulfide nanoparticles for methanol dehydrogenation, *J. Phys. Chem. B* 108 (2004) 18670–18674.
- [16] M. Sathish, B. Viswanathan, R.P. Viswanath, Alternate synthetic strategy for the preparation of CdS nanoparticles and its exploitation for water splitting, *Int. J. Hydrogen Energy* 31 (2006) 891–898.
- [17] X. Fu, D. Wang, J. Wang, H. Shi, C. Song, High aspect ratio CdS nanowires synthesized in microemulsion system, *Mater. Res. Bull.* 39 (2004) 1869–1874.
- [18] D. Mo, J. Liu, H.J. Yao, J.L. Duan, M.D. Hou, Y.M. Sun, Y.F. Chen, Z.H. Xue, L. Zhang, Preparation and characterization of CdS nanotubes and nanowires by electrochemical synthesis in ion-track templates, *J. Cryst. Growth* 310 (2008) 612–616.
- [19] J.K. Dongre, V. Nogriya, M. Ramrakhiani, Structural, optical and photoelectrochemical characterization of CdS nanowire synthesized by chemical bath deposition and wet chemical etching, *Appl. Surf. Sci.* 255 (2009) 6115–6120.
- [20] T. Zhai, X. Fang, Y. Bando, Q. Liao, X. Xu, H. Zeng, Y. Ma, J. Yao, D. Golberg, Morphology-dependent stimulated emission and field emission of ordered CdS nanostructure arrays, *ACS Nano* 3 (2009) 949–959.
- [21] C.J. Barrelet, Y. Wu, D.C. Bell, C.M. Lieber, Synthesis of CdS and ZnS nanowires using single-Source molecular precursors, *J. Am. Chem. Soc.* 125 (2003) 11498–11499.
- [22] Y. Li, Y. Hu, S. Peng, G. Lu, S. Li, Synthesis of CdS nanorods by an ethylenediamine assisted hydrothermal method for photocatalytic hydrogen evolution, *J. Phys. Chem. C* 113 (2009) 9352–9358.
- [23] S. Xiong, B. Xi, C. Wang, G. Zou, L. Fei, W. Wang, Y. Qian, Shape-controlled synthesis of 3D and 1D structures of CdS in a binary solution with L-cysteine's assistance, *Chemistry* 13 (2007) 3076–3081.
- [24] P. Dalvand, M.R. Mohammadi, Controlling morphology and structure of nanocrystalline cadmium sulfide (CdS) by tailoring solvothermal processing parameters, *J. Nanopart. Res.* 13 (2011) 3011–3018.
- [25] G. Demazeau, Solvothermal processes: new trends in materials chemistry, *J. Phys.: Conf. Ser.* 121 (2008) 082003.
- [26] W. Qingqing, X. Gang, H. Gaorong, Solvothermal synthesis and characterization of uniform CdS nanowires in high yield, *J. Solid State Chem.* 178 (2005) 2680–2685.
- [27] Z. Guifu, L. Hui, Z. Yuanguang, X. Kan, Q. Yitai, Solvothermal/hydrothermal route to semiconductor nanowires, *Nanotechnology* 17 (2006) S313.
- [28] F. Vaquero, J.G. Fierro, R. Navarro Yerga, From nanorods to nanowires of CdS synthesized by a solvothermal method: influence of the morphology on the photoactivity for hydrogen evolution from water, *Molecules* 21 (2016) 401.
- [29] F. Vaquero, R.M. Navarro, J.L.G. Fierro, Evolution of the nanostructure of CdS using solvothermal synthesis at different temperature and its influence on the photoactivity for hydrogen production, *Int. J. Hydrogen Energy* 41 (2016) 11558–11567.
- [30] J. Yu, Y. Yu, B. Cheng, Enhanced visible-light photocatalytic H_2 -production performance of multi-armed CdS nanorods, *RSC Adv.* 2 (2012) 11829–11835.
- [31] J. Yu, Y. Yu, P. Zhou, W. Xiao, B. Cheng, Morphology-dependent photocatalytic H_2 -production activity of CdS, *Appl. Catal. B: Environ.* 156–157 (2014) 184–191.
- [32] J. Jin, J. Yu, G. Liu, P.K. Wong, Single crystal CdS nanowires with high visible-light photocatalytic H_2 -production performance, *J. Mater. Chem. A* 1 (2013) 10927–10934.
- [33] A. Hernández-Gordillo, F. Tzompantzi, S. Oros-Ruiz, L.M. Torres-Martínez, R. Gómez, Enhanced blue-light photocatalytic H_2 production using CdS nanofiber, *Catal. Commun.* 45 (2014) 139–143.
- [34] D. Wang, D. Li, L. Guo, F. Fu, Z. Zhang, Q. Wei, Template-free hydrothermal synthesis of novel three-dimensional dendritic CdS nanoarchitectures, *J. Phys. Chem. C* 113 (2009) 5984–5990.
- [35] W.-T. Yao, S.-H. Yu, S.-J. Liu, J.-P. Chen, X.-M. Liu, F.-Q. Li, Architectural control synthesis of CdS and CdSe nanoflowers, branched nanowires, and nanotrees via a solvothermal approach in a mixed solution and their photocatalytic property, *J. Phys. Chem. B* 110 (2006) 11704–11710.
- [36] Z. Wang, L. Pan, L. Wang, H. Wang, Urchin-like CdS microspheres self-assembled from CdS nanorods and their photocatalytic properties, *Solid State Sci.* 13 (2011) 970–975.
- [37] J.S. Jang, U.A. Joshi, J.S. Lee, Solvothermal synthesis of CdS nanowires for photocatalytic hydrogen and electricity production, *J. Phys. Chem. C* 111 (2007) 13280–13287.
- [38] G. Demazeau, Solvothermal processes: definition, key factors governing the involved chemical reactions and new trends, *Zeitschrift für Naturforschung B* 65 (2010) 999–1006.
- [39] F.H. Zhao, Q. Su, N.S. Xu, C.R. Ding, M.M. Wu, Selectively hydrothermal and solvothermal growth of CdS nanospheres and nanorods: a facile way to tune finely optical properties, *J. Mater. Sci.* 41 (2016) 1449–1454.

- [40] D. Lang, Q. Xiang, G. Qiu, X. Feng, F. Liu, Effects of crystalline phase and morphology on the visible light photocatalytic H₂-production activity of CdS nanocrystals, *Dalton Trans.* 43 (2014) 7245–7253.
- [41] C.D. Wagner, L.E. Davis, M.V. Zeller, J.A. Taylor, R.H. Raymond, L.H. Gale, Empirical atomic sensitivity factors for quantitative analysis by electron spectroscopy for chemical analysis, *Surf. Interface Anal.* 3 (1981) 211–225.
- [42] R. Thiruvengadathan, O. Regev, Hierarchically ordered cadmium sulfide nanowires dispersed in aqueous solution, *Chem. Mater.* 17 (2005) 3281–3287.
- [43] J.F. Reber, K. Meier, Photochemical production of hydrogen with zinc sulfide suspensions, *J. Phys. Chem.* 88 (1984) 5903–5913.
- [44] S. Wageh, M. Maize, S. Han, A.A. Al-Ghamdi, X. Fang, Effect of solvent and environmental conditions on the structural and optical properties of CdS nanoparticles, *RSC Adv.* 4 (2014) 24110–24118.
- [45] A. Hernández-Gordillo, S. Oros-Ruiz, R. Gómez, Preparation of efficient cadmium sulfide nanofibers for hydrogen production using ethylenediamine (NH₂CH₂CH₂NH₂) as template, *J. Colloid Interface Sci.* 451 (2015) 40–45.
- [46] X. Wang, Z. Feng, D. Fan, F. Fan, C. Li, Shape-Controlled synthesis of CdS nanostructures via a solvothermal method, *Crystal Growth Des.* 10 (2010) 5312–5318.
- [47] J. Yang, J.-H. Zeng, S.-H. Yu, L. Yang, G.-e. Zhou, Y.-t. Qian, Formation process of CdS nanorods via solvothermal route, *Chem. Mater.* 12 (2000) 3259–3263.
- [48] H. Cao, G. Wang, S. Zhang, X. Zhang, D. Rabinovich, Growth and optical properties of wurtzite-type CdS nanocrystals, *Inorg. Chem.* 45 (2006) 5103–5108.
- [49] P. Nandakumar, C. Vijayan, M. Rajalakshmi, A.K. Arora, Murti YVGS, Raman spectra of CdS nanocrystals in Nafion: longitudinal optical and confined acoustic phonon modes, *Physica E* 11 (2001) 377–383.
- [50] S. Rengaraj, S. Venkataraj, S.H. Jee, Y. Kim, C.-w. Tai, E. Repo, A. Koistinen, A. Ferancova, M. Sillanpää, Cauliflower-like CdS microspheres composed of nanocrystals and their physicochemical properties, *Langmuir* 27 (2011) 352–358.
- [51] D.R.T. Zahn, C. Maierhofer, A. Winter, M. Reckzügel, R. Srama, A. Thomas, K. Horn, W. Richter, The growth of cubic CdS on InP(110) studied insitu by Raman spectroscopy, *J. Vac. Sci. Technol. B* 9 (1991) 2206–2211.
- [52] O. Zelaya-Angel, F.d.L. Castillo-Alvarado, J. Avendaño-López, A. Escamilla-Esquivel, G. Contreras-Puente, R. Lozada-Morales, G. Torres-Delgado, Raman studies in CdS thin films in the evolution from cubic to hexagonal phase, *Solid State Commun.* 104 (1997) 161–166.
- [53] A. Pan, R. Liu, Q. Yang, Y. Zhu, G. Yang, B. Zou, K. Chen, Stimulated emissions in aligned CdS nanowires at room temperature, *J. Phys. Chem. B* 109 (2005) 24268–24272.
- [54] Y. Wang, G. Meng, L. Zhang, C. Liang, J. Zhang, Catalytic growth of large-scale single-crystal CdS nanowires by physical evaporation and their photoluminescence, *Chem. Mater.* 14 (2002) 1773–1777.
- [55] C.A. Arguello, D.L. Rousseau, Porto SPS, first-order Raman effect in wurtzite-type crystals, *Phys. Rev.* 181 (1969) 1351–1363.
- [56] L. Zeiri, I. Patla, S. Acharya, Y. Golan, S. Efrima, Raman spectroscopy of ultranarrow CdS nanostructures, *J. Phys. Chem. C* 111 (2007) 11843–11848.
- [57] M.A. Mahdi, J.J. Hassan, S.J. Kasim, S.S. Ng, S.S. Hassan, Solvothermal growth of single-crystal CdS nanowires, *Bull. Mater. Sci.* 37 (2014) 337–345.
- [58] M.A. Mahdi, J.J. Hassan, S.S. Ng, Z. Hassan, Growth of CdS nanosheets and nanowires through the solvothermal method, *J. Cryst. Growth* 359 (2012) 43–48.
- [59] I.H. Campbell, P.M. Fauchet, The effects of microcrystal size and shape on the one phonon Raman spectra of crystalline semiconductors, *Solid State Commun.* 58 (1986) 739–741.
- [60] F. Widulle, S. Kramp, N.M. Pyka, A. Göbel, T. Ruf, A. Debernardi, R. Lauck, M. Cardona, The phonon dispersion of wurtzite CdSe, *Physica B* 263–264 (1999) 448–451.
- [61] M. Thommes, K. Kaneko, V. Neimark Alexander, P. Olivier James, F. Rodriguez-Reinoso, J. Rouquerol, S.W. Sing Kenneth, Physiosorption of gases, with special reference to the evaluation of surface area and pore size distribution (IUPAC Technical Report), *Pure Appl. Chem.* 87 (2015) 1051–1069.
- [62] R. Chen, J. Yu, W. Xiao, Hierarchically porous MnO₂ microspheres with enhanced adsorption performance, *J. Mater. Chem. A* 1 (2013) 11682–11690.
- [63] Q. Xiang, B. Cheng, J. Yu, Hierarchical porous CdS nanosheet-assembled flowers with enhanced visible-light photocatalytic H₂-production performance, *Appl. Catal. B: Environ.* 138–139 (2013) 299–303.
- [64] D.S. Kim, Y.J. Cho, J. Park, J. Yoon, Y. Jo, M.-H. Jung, (Mn Zn) Co-doped CdS nanowires, *J. Phys. Chem. C* 111 (2007) 10861–10868.
- [65] D. Mayer, K.H. Hallmeier, T. Chassé, R. Szargan, SXPS analysis of passivation and complexation on the CdS (101–0) surface, *Fresenius' J. Anal. Chem.* 361 (1998) 689–692.
- [66] X. Ma, F. Xu, Y. Liu, X. Liu, Z. Zhang, Y. Qian, Double-dentate solvent-directed growth of multi-armed CdS nanorod-based semiconductors, *Mater. Res. Bull.* 40 (2005) 2180–2188.
- [67] S. Li, L. Zhang, T. Jiang, L. Chen, Y. Lin, D. Wang, T. Xie, Construction of shallow surface states through light Ni doping for high-efficiency photocatalytic hydrogen production of CdS nanocrystals, *Chemistry* 20 (2014) 311–316.
- [68] M. Marychurch, G.C. Morris, X-ray photoelectron spectra of crystal and thin film cadmium sulphide, *Surf. Sci.* 154 (1985) L251–L254.
- [69] P.V. Kamat, N.M. Dimitrijevic, R.W. Fessenden, Photoelectrochemistry in particulate systems. 6. Electron-transfer reactions of small cadmium sulfide colloids in acetonitrile, *J. Phys. Chem.* 91 (1987) 396–401.
- [70] G.Q. Xu, B. Liu, S.J. Xu, C.H. Chew, S.J. Chua, L.M. Gana, Luminescence studies of CdS spherical particles via hydrothermal synthesis, *J. Phys. Chem. Solids* 61 (2000) 829–836.
- [71] Q. Pan, K. Huang, S. Ni, Q. Wang, F. Yang, D. He, Fabrication and photoluminescence properties of large-scale hierarchical CdS dendrites, *Mater. Lett.* 61 (2007) 4773–4776.
- [72] L. Spanhel, M. Haase, H. Weller, A. Henglein, Photochemistry of colloidal semiconductors. 20. Surface modification and stability of strong luminescing CdS particles, *J. Am. Chem. Soc.* 109 (1987) 5649–5655.
- [73] O. Takaaki, K. Shin-ichi, M. Kiyoto, O. Seinosuke, A. Toshihiro, Photoluminescence of CdS nanoparticles suspended in vacuum and its temperature increase by laser irradiation, *J. Phys.: Condens. Matter* 14 (2002) 9743.
- [74] W.-S. Chae, J.-H. Ko, I.-W. Hwang, Y.-R. Kim, Emission characteristics of CdS nanoparticles induced by confinement within MCM-41 nanotubes, *Chem. Phys. Lett.* 365 (2002) 49–56.
- [75] J. Zhang, L. Sun, C. Liao, C. Yan, Size control and photoluminescence enhancement of CdS nanoparticles prepared via reverse micelle method, *Solid State Commun.* 124 (2002) 45–48.
- [76] W. Wang, I. Germanenko, M.S. El-Shall, Room-Temperature synthesis and characterization of nanocrystalline CdS, ZnS, and cdxZn1-xS, *Chem. Mater.* 14 (2002) 3028–3033.
- [77] D.C. Onwudiwe, C.A. Strydom, O.S. Oluwafemi, Effect of some nitrogen donor ligands on the optical and structural properties of CdS nanoparticles, *New J. Chem.* 37 (2013) 834–842.
- [78] Z. López-Cabaña, C.M. Sotomayor Torres, G. González, Semiconducting properties of layered cadmium sulphide-based hybrid nanocomposites, *Nanoscale Res. Lett.* 6 (2011) 1–8.
- [79] G.A.M. Ali, O.A. Fouad, S.A. Makhlof, Structural, optical and electrical properties of sol-gel prepared mesoporous Co₃O₄/SiO₂ nanocomposites, *J. Alloys Compd.* 579 (2013) 606–611.
- [80] R. Gaur, P. Jeevanandam, Effect of anions on the morphology of CdS nanoparticles prepared via thermal decomposition of different cadmium thiourea complexes in a solvent and in the solid state, *New J. Chem.* 39 (2015) 9442–9453.
- [81] S.K. O'Leary, S. Zukotynski, J.M. Perz, Disorder and optical absorption in amorphous silicon and amorphous germanium, *J. Non-Cryst. Solids* 210 (1997) 249–253.
- [82] P. Zhao, K. Huang, Preparation and characterization of netted sphere-like CdS nanostructures, *Crystal Growth Des.* 8 (2007) 717–722.
- [83] L.E. Brus, Electron-electron and electron-hole interactions in small semiconductor crystallites: the size dependence of the lowest excited electronic state, *J. Chem. Phys.* 80 (1984) 4403–4409.
- [84] J. Zhang, S. Wageh, A. Al-Ghamdi, J. Yu, New understanding on the different photocatalytic activity of wurtzite and zinc-blende CdS, *Appl. Catal. B: Environ.* 192 (2016) 101–107.
- [85] S.-H. Yu, J. Yang, Z.-H. Han, Y. Zhou, R.-Y. Yang, Y.-T. Qian, Y.-H. Zhang, Controllable synthesis of nanocrystalline CdS with different morphologies and particle sizes by a novel solvothermal process, *J. Mater. Chem.* 9 (1999) 1283–1287.
- [86] C.H. Rhee, J.S. Lee, S.H. Chung, Synthesis of nitrogen-doped titanium oxide nanostructures via a surfactant-free hydrothermal route, *J. Mater. Res.* 20 (2005) 3011–3020.
- [87] R.M. Navarro, F. del Valle, J.A. Villoria de la Mano, M.C. Álvarez-Galván, J.L.G. Fierro, Photocatalytic water splitting under visible light: concept and catalysts development, in: I.d.L. Hugo, R. BenitoSerrano (Eds.), *Advances in Chemical Engineering*, Academic Press, 2009, 2016, pp. 111–143.
- [88] D. Zhao, Q. Wu, C. Yang, R.T. Koodali, Visible light driven photocatalytic hydrogen evolution over CdS incorporated mesoporous silica derived from MCM-48, *Appl. Surf. Sci.* 356 (2015) 308–316.
- [89] M. Matsumura, S. Furukawa, Y. Saho, H. Tsubomura, Cadmium sulfide photocatalyzed hydrogen production from aqueous solutions of sulfite: effect of crystal structure and preparation method of the catalyst, *J. Phys. Chem.* 89 (1985) 1327–1329.
- [90] Q. Xiao, C. Xiao, Surface-defect-states photoluminescence in CdS nanocrystals prepared by one-step aqueous synthesis method, *Appl. Surf. Sci.* 255 (2009) 7111–7114.
- [91] X. Li, J. Yu, M. Jaroniec, Hierarchical photocatalysts, *Chem. Soc. Rev.* 45 (2016) 2603–2636.
- [92] P. Chang, H. Cheng, W. Li, L. Zhuo, L. He, Y. Yu, F. Zhao, Photocatalytic reduction of o-chloronitrobenzene under visible light irradiation over CdS quantum dot sensitized TiO₂, *Phys. Chem. Chem. Phys.* 16 (2014) 16606–16614.
- [93] C. Eley, T. Li, F. Liao, S.M. Fairclough, J.M. Smith, G. Smith, S.C.E. Tsang, Nanofunction-Mediated photocatalytic enhancement in heterostructured CdS/ZnO, CdSe/ZnO, and CdTe/ZnO nanocrystals, *Angew. Chem. Int. Ed.* 53 (2014) 7838–7842.
- [94] M. Fu, Q. Jiao, Y. Zhao, One-step vapor diffusion synthesis of uniform CdS quantum dots/reduced graphene oxide composites as efficient visible-light photocatalysts, *RSC Adv.* 4 (2014) 23242–23250.
- [95] Q. Li, X. Li, S. Wageh, A.A. Al-Ghamdi, J. Yu, CdS/Graphene nanocomposite photocatalysts, *Adv. Energy Mater.* 5 (2015), 1500010-n/a.
- [96] L. Ge, F. Zuo, J. Liu, Q. Ma, C. Wang, D. Sun, L. Bartels, P. Feng, Synthesis and efficient visible light photocatalytic hydrogen evolution of polymeric g-C₃N₄ coupled with CdS quantum dots, *J. Phys. Chem. C* 116 (2012) 13708–13714.

- [97] P.D. Cozzoli, A. Kornowski, H. Weller, Low-temperature synthesis of soluble and processable organic-capped anatase TiO₂ nanorods, *J. Am. Chem. Soc.* 125 (2003) 14539–14548.
- [98] A.E. Saunders, A. Ghezelbash, P. Sood, B.A. Korgel, Synthesis of high aspect ratio quantum-size CdS nanorods and their surface-dependent photoluminescence, *Langmuir* 24 (2008) 9043–9049.
- [99] J.-J. Zhou, R. Wang, X.-L. Liu, F.-M. Peng, C.-H. Li, F. Teng, Y.-P. Yuan, In situ growth of CdS nanoparticles on UiO-66 metal-organic framework octahedrons for enhanced photocatalytic hydrogen production under visible light irradiation, *Appl. Surf. Sci.* 346 (2015) 278–283.